ADVANCED OPTICAL MATERIALS
www.advopticalmat.de

Forward Brillouin Scattering Spectroscopy in Optical Fibers with Whispering-Gallery Modes

Luís A. Sánchez, Martina Delgado-Pinar, Antonio Díez, and Miguel V. Andrés*

Opto-mechanical interactions in different photonic platforms as optical fibers and optical microresonators are raising great attention, and new exciting achievements have been reported in the last few years. Transverse acoustic mode resonances (TAMRs) in optical fibers –which can be excited optically via electrostriction and generate forward Brillouin scattering (FBS)– are being promoted as the physical mechanism for new fiber-sensing concepts. Here, the study reports a novel approach to detect and characterize opto-excited TAMRs of an optical fiber based on the interplay with optical surface wave resonances, i.e., optical whispering-gallery mode (WGM) resonances. TAMRs induce perturbations in the geometry and the dielectric permittivity of the fiber over the entire cross-section. It is shown that these perturbations couple the acoustic with the optical resonances and affect WGMs in a noticeable way. The study proposes and demonstrates the use of WGMs for probing opto-excited TAMRs in optical fibers. This probing technique provides the narrowest linewidths ever reported for the TAMRs and demonstrates an optimum efficiency for the detection of low-order TAMRs. The interplay between sensitivity, bandwidth, and Q factor of the WGM resonance is discussed.

1. Introduction

Interplay between optical and acoustic traveling waves in optical waveguides, such as optical fibers, has been exploited in the past to develop a number of applications[1–5] and devices.[6,7] Opto-mechanical interactions between optical and acoustic resonances have also been investigated in wavelength-scale photonic structures, mostly in three-dimensional microresonators such as toroids,[8] spheres,[9] and microbubbles.[10] In most previous works, acoustic resonances of the microresonator are stimulated by the optical resonances (i.e., optical whispering-gallery-modes (WGMs)) via radiation pressure. In those structures, such physical mechanism benefits from the very high-Q factor of optical WGMs that enables large optical energy density storage inside the microresonator (MR).

In this paper, we exploit, the interplay between optical and acoustic resonances in standard optical fibers. Optical fibers are primarily a waveguide, but also a cylindrical microresonator for both, optical and acoustic oscillations. In particular, we demonstrate the use of optical resonances, i.e., WGMs, to perform modal spectroscopy investigation of opto-excited transverse acoustic mode resonances (TAMRs) of an optical fiber.

Optical WGM resonances are electromagnetic resonances of surface waves guided by curvature that exist in circularly symmetric dielectric resonators. They exhibit very high-Q values and their fields are tightly confined near the surface of the resonator. The outstanding properties of WGM resonances in optical microcavities with different shapes have been the basis for the development of impressive achievements in many areas, such as nonlinear photonics,[11] laser technologies,[12–13] or sensing.[14] In standard optical fibers, the quality factor of WGM resonances can be in the order $\approx 10^7$, which means that the spectral bandwidth of the resonances in the C-band can be in the order of few tens of fm. WGMs of optical fibers have been successfully used to investigate different properties of the optical fiber itself, such as the anisotropy of the elasto-optic effect,[15] and thermal effects in active fibers and fiber optic components.[16,17]

A particular type of opto-mechanical interaction is forward Brillouin scattering (FBS). FBS refers to the interaction of an optical signal with opto-excited acoustic modes. It is widely investigated in optical fibers,[18–20] and other photonic platforms.[21,22] In the context of optical fibers, FBS raises increasing interest in recent years related with potential applications for sensing.[23–27] It enables, for instance, the analysis of media outside the fiber, even through the fiber coating.[28] Distributed sensing based on FBS has also been demonstrated.[29–32] Additionally, FBS provides a precise tool to characterize the elastic and the

L. A. Sánchez, M. Delgado-Pinar, A. Díez, M. V. Andrés
Laboratory of Fiber Optics
ICMUV
Universidad de Valencia
Burjassot 46100, Spain
E-mail: antonio.diez@uv.es
M. Delgado-Pinar, A. Díez, M. V. Andrés
Departamento de Física Aplicada y Electromagnetismo
Universidad de Valencia
Burjassot 46100, Spain

The ORCID identification number(s) for the author(s) of this article can be found under https://doi.org/10.1002/adom.202301629

DOI: 10.1002/adom.202301629

geometric properties of optical fibers; Poisson's ratio with unprecedented accuracy has been reported,[33] and non-destructive and distributed measurement of fiber diameter with nanometer resolution has also been demonstrated.[34] Recently, the first optical fiber laser based on inter-modal FBS has been reported.[35]

The acoustic waves involved in FBS are nearly transverse modes. The oscillation of TAMRs in optical waveguides can be stimulated by guided optical waves through the mechanism of electrostriction. In an optical fiber, which acoustically can be considered as a long, homogeneous solid silica cylinder, the vibrational modes behind this interaction are the axially symmetric $R_{0,p}$ radial modes and the axially asymmetric $TR_{2,p}$ torsional-radial modes.[18]

The development of applications based on this nonlinear effect requires accurate knowledge of the properties of such acoustic modes. In optical fibers, radial modes give rise to only phase modulation of the guided light, while torsional-radial modes cause also light depolarization. Thus, $TR_{2,p}$ modes are easier to investigate using polarization modulation techniques.[18] However, $R_{0,p}$ modes are in practice more interesting, since they yield to stronger and polarization-independent interactions with the fundamental fiber mode. The most widespread method for the experimental characterization of $R_{0,p}$ modes in optical fibers is based on optical interferometry.[19] Since the scattering efficiency of TAMRs is very weak, interferometric methods require long interaction lengths to provide sufficient sensitivity, tens or even hundreds of meters of fiber. However, the use of such long fibers results in spectral broadening of the acoustic resonances. An alternative phase demodulation technique based on a narrowband fiber-Bragg grating (FBG) was demonstrated.[36] A different approach recently reported is based on the interaction of TAMRs with a grating written in the core of the fiber under test (FUT). Demonstrations using LPGs,[37] and FBGs[38] have been reported. Using short lengths of fiber, this method reduces the linewidth broadening due to fiber inhomogeneity, and the acoustic resonances exhibited a linewidth close to the theoretical limit.

With the exception of experiments performed in multi-core optical fibers,[26,38] all the methods reported so far are based on a pump-and-probe scheme, in which both, the pump and the probe beams propagate in the core of the FUT. Some drawbacks arise from this feature. Cross-phase modulation (XPM) is induced by the optical pump due to the instantaneous Kerr effect. Then, time-gating of the probe signal is required to avoid some unwanted effects like the asymmetric shape of the resonances, which was shown to be produced by the interference between FBS and the optical Kerr effect.[39] Moreover, the optical signal must be processed before it is photodetected in order to filter out the pump from the probe signal. This normally involves the insertion of extra optical components in the experimental implementation.

In this paper, we report a rather different approach based on the use of optical WGM resonances, while TAMRs are excited by an optical pump that propagates in the fiber core. These acoustic modes induce fiber perturbations that extend across the entire fiber, which enables to be interrogated with the assistance of an optical WGM resonance, whose fields are tightly confined close to the fiber surface. In the present approach, therefore, pump and probe optical waves do not physically overlap, thus, optical XPM does not occur. Additionally, the probe beam is coupled to the WGM of the FUT via the evanescent field of an auxiliary thin tapered fiber (a simple fiber tip could be used as well[40]). Therefore, pump and probe signals propagate in different fibers, thus no filtering of the optical signal is required.

We show that WGMs are only sensitive to radial modes but not to torsional-radial modes. Namely, the torsional-radial modes, although excited by the pump, are not detected by the probe signal. Then, the probe signal do naturally contains only the contribution of $R_{0,p}$ modes. Therefore, polarization control or polarization scrambling of the pump to suppress torsional-radial modes is not required. Furthermore, it is shown that the relative amplitude with which different TAMRs are detected is rather different than in previous methods in which the probe propagates in the fiber core.

2. Principles of Operation

It is known that an optical fiber can also be regarded as a cylindrical optical microresonator that supports high-Q optical WGM resonances. For a bare optical fiber immersed in air, the resonance wavelength of such WGMs depend on two fiber properties, i. e., the fiber radius and the cladding refractive index. When a change of any of these two magnitudes is produced, the resonance wavelength of such WGMs will shift.

The excitation of transverse acoustic mode resonances in an optical fiber introduces a time-dependent perturbation of both key quantities. First, a TAMR causes a perturbation of the refractive index due to the photo-elastic effect (hereinafter called "material perturbation"). The profile across the optical fiber of such refractive index perturbation is determined by the strain field of the TAMR. Second, the cross section of the fiber is also slightly modulated (hereinafter called "geometrical perturbation"), according to the displacement vector of the corresponding TAMR.

The contribution of the material perturbation to the WGM wavelength shift caused by a TAMR is ruled by the overlapping between such perturbation and the WGM fields. Since WGM fields are tightly confined around the outer surface of the fiber –they extend inside the fiber just few microns–, the WGM shift caused by the material perturbation will depend on the magnitude of the perturbation near the surface. Note that this is different to most previously reported methods in which TAMRs are probed by an optical beam propagating through the fiber core where the magnitude of the material perturbation is larger. As it will be shown below, the refractive index perturbations near the fiber surface are much weaker than in the fiber core. Therefore, the effect of the material perturbation produced by the TAMR on a probe optical beam whose fields overlap the core area is stronger than when they extend near the surface. This apparent weakness of the WGMs-based probing method reported here is counteracted by the extremely narrowband resonances of WGMs, which enables an extremely low detection limit. In practical implementations, a WGM wavelength shift in order of ≈fm can readily be detected.

In optical fibers, FBS is caused by the excitation of two types of TAMRs, i.e., radial $R_{0,p}$ modes and torsional-radial modes of the family $TR_{2,p}$. The displacement vector that describes $R_{0,p}$ modes only contains the radial component, which depends only on the radial coordinate r, being independent on the azimuthal angle ϕ. The excitation of $R_{0,p}$ modes of an optical fiber by a Gaussian opti-

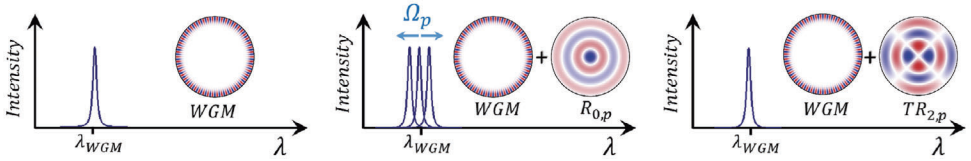

Figure 1. Schematic illustration of the operation principle. Fields' patterns of representative optical WGM, and $R_{0,p}$ and $TR_{2,p}$ acoustic modes are shown. The oscillation of a radial acoustic mode modulates the WGM resonance wavelength at the resonance frequency of the $R_{0,p}$ mode, Ω_p. The amplitude of the WGM spectral oscillation is determined by the amplitude of the $R_{0,p}$ mode fields. On the contrary, the oscillation of a torsional-radial mode does not affect the WGM resonance wavelength.

cal pump beam propagating in the fundamental mode of the fiber is discussed in detail in Supporting information. On the contrary, the components of the displacement vector of $TR_{2,p}$ modes do change periodically with the azimuthal angle, more specifically, they change harmonically with twice the azimuthal angle. Such angular dependence is translated into the perturbations of refractive index and radius. This results into a quite interesting feature, which is that WGMs are insensitive to $TR_{2,p}$ modes, at least for small perturbations (see Supporting information for further details). **Figure 1** illustrates the operation principle. In the following sections, we will describe in detail the bases that support the probing technique of TAMRs in optical fibers with WGMs.

2.1. WGM Wavelength Shift Due To $R_{0,p}$-Induced Fiber Material Perturbation

The strain field associated to the displacement vector of an acoustic mode produces a perturbation of the refractive index across the optical fiber due to the photo-elastic effect. For $R_{0,p}$ modes, only two components of strain are different from zero, that is the strain components in the radial direction $S_{rr}^{(p)}$, and in the azimuthal direction $S_{\phi\phi}^{(p)}$. Such strain components cause the perturbation of the three diagonal elements of the local dielectric tensor –the radial, the azimuthal, and the axial component– while the off-diagonal elements are not changed. The specific expressions for evaluating $S_{rr}^{(p)}$ and $S_{\phi\phi}^{(p)}$ of $R_{0,p}$ modes, and the perturbations of the relative dielectric tensor elements $\delta\varepsilon_{rr}^{(p)}$, $\delta\varepsilon_{\phi\phi}^{(p)}$ and, $\delta\varepsilon_{zz}^{(p)}$, as well as details of the radial profile of such quantities are included in Supporting information.

The magnitude of the changes produced by the oscillation of a TAMR in the different refractive index tensor components is actually small, in the order of $\approx 10^{-10}$ according to calculations performed for our experimental conditions when considering the highest pump power available, 6 kW (see, Figure S2c,d, Supporting information). Additionally, $R_{0,p}$ modes do not deform the cross section of the fiber. Consequently, it has been assumed that $R_{0,p}$ only causes the shift of the WGM resonance wavelength, without affecting the intrinsic quality factor. Thus, accurate calculation of the WGM wavelength shift was performed by a perturbative approach that takes into account the tensor character of the permittivity. The relative WGM wavelength shift owing to the change of permittivity induced in the fiber by the $R_{0,p}$ mode can be calculated by,[41]

$$\left.\frac{\delta\lambda^{(p)}}{\lambda_0}\right|_{\delta\varepsilon} \approx \frac{\int_{\mathbb{R}^3}\left(\varepsilon_0\cdot\delta\varepsilon^{(p)}\cdot\vec{E}\cdot\vec{E}^*\right)dV}{\int_{\mathbb{R}^3}\left(\varepsilon_0\varepsilon\cdot\vec{E}\cdot\vec{E}^*+\mu_0\cdot\vec{H}\cdot\vec{H}^*\right)dV} \quad (1)$$

where $\vec{E}$ and $\vec{H}$ are the electric and magnetic fields of the WGM, λ_0 is the resonance wavelength of the WGM in absence of perturbation, ϵ is the relative permittivity, ϵ_0 and μ_0 are the dielectric permittivity and magnetic permeability in vacuum, respectively, and $\delta\epsilon^{(p)}$ is a tensor that contains the different components of the perturbation of the relative permittivity. The numerator represents the overlap integral between the perturbation and the WGM fields. The integrand may be written as,

$$\delta\varepsilon^{(p)}\cdot\vec{E}\cdot\vec{E}^* = \delta\varepsilon_{rr}^{(p)}\cdot|e_r|^2 + \delta\varepsilon_{\phi\phi}^{(p)}\cdot|e_\phi|^2 + \delta\varepsilon_{zz}^{(p)}\cdot|e_z|^2 \quad (2)$$

where e_r, e_ϕ and e_z are the radial, azimuthal, and axial components of the WGM electric field, respectively. According to the WGMs fields' structure,[15,42] both *TE*- and *TM*-polarized WGMs will be sensitive to the perturbation in the dielectric permittivity, but in a different way. In a cylindrical microresonator, the electric field of *TM*-polarized WGMs involves only one component, which is the axial e_z component, while the electric field of *TE*-polarized WGMs involves the two components that are transverse to the fiber axis, that is, e_r and e_ϕ. Therefore, the shift of *TM*-polarized WGMs depends only on $\delta\varepsilon_{zz}^{(p)}$, while in the case of *TE*-polarized WGMs it is determined by the perturbation of the dielectric components in the transverse plane $\delta\varepsilon_{rr}^{(p)}$ and $\delta\varepsilon_{\phi\phi}^{(p)}$.

The strain field of a given TAMR oscillates harmonically with time, consequently, the resonance wavelength of the WGM does so, with the corresponding amplitude. Following the notation used in Section S1 (Supporting information), the relative resonance wavelength shift can be expressed as,

$$\left.\frac{\delta\lambda^{(p)}}{\lambda_0}\right|_{\delta\varepsilon} \equiv C_0^{(p)}\cdot e^{-\gamma_p\cdot t}\cdot e^{-j\Omega_p\cdot t} \quad (3)$$

where $C_0^{(p)}$ is the magnitude of the relative wavelength shift that results from the material contribution, Ω_p and γ_p are the resonance frequency and the attenuation coefficient of the $R_{0,p}$ mode, respectively. The attenuation coefficient is related with the spectral bandwidth Γ_p of the resonance, being $\gamma_p = \Gamma_p/2$. **Figure 2**a shows the values of $C_0^{(p)}$ that result from the oscillation of the $R_{0,p}$ modes excited by an optical pump pulse. The excitation conditions of the $R_{0,p}$ acoustic modes taken into account in these calculations are representative of the experimental conditions, and are the same as in the calculations included in Section S1 (Supporting information). In particular, we show the effect on the $TE_{358,1}$ and the $TM_{358,1}$ WGMs, since they are the WGMs used in the experimental demonstration. For almost all $R_{0,p}$ modes, the wavelength shift amplitude is larger for *TM*- than for *TE*-polarized WGM resonances. Notice that the wavelength shift produced by

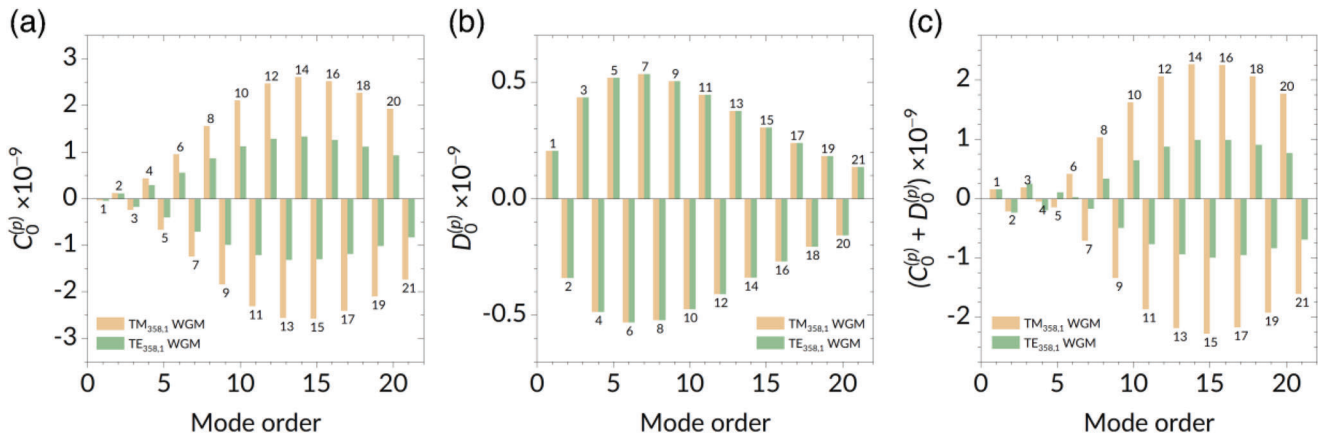

Figure 2. Amplitude of the relative wavelength shift of $TE_{358,1}$ and $TM_{358,1}$ WGMs produced by the oscillation of different $R_{0,p}$ acoustic modes excited by a pump pulse. Contribution due to a) the material perturbation, b) the geometrical perturbation, and c) the overall values. The order p of the radial acoustic modes is indicated. In the simulations, the pump pulse taken was a sech^2-shaped pulse of 700 ps duration and 6 kW peak power, and the modal diameter of the pump beam was 3.5 µm.

$R_{0,p}$ modes with even p order is π phase-shifted with respect to that produced by $R_{0,p}$ modes with odd p order. From low to high mode order p, the magnitude of the WGM resonance shift increases with the mode number up to the $R_{0,14}$ mode, which produces the largest relative wavelength shift, and then it decays with the mode order.

Finally, we may comment that the magnitude of the WGM wavelength shift changes, as well, with the radial order of the WGM resonance. This is due to the different radial profile of their electromagnetic fields, so the overlap with the refractive index perturbation is also different.

2.2. WGM Wavelength Shift Due to $R_{0,p}$-Induced Fiber Geometrical Perturbation

Given the characteristics of its displacement vector, the oscillation of an $R_{0,p}$ mode introduces a perturbation in the fiber radius while the circular shape of the fiber cross-section is preserved. The amplitude of the wavelength shift of *TE*- and *TM*-polarized WGM resonances due to the radius perturbation caused by the oscillation of an $R_{0,p}$ acoustic mode was obtained by numerically solving the corresponding characteristic equations for *TE*- and *TM*-polarized WGM resonances of a dielectric silica cylinder immersed in air.[41] First, the resonance wavelengths were calculated for a cylinder of radius a, and then for a cylinder of radius $a + \delta a_0^{(p)}$, where $\delta a_0^{(p)}$ is the magnitude of the radius perturbation produced by the $R_{0,p}$ mode (see Supporting information). The resulting WGM relative wavelength shift that results from the radius perturbation can be expressed as follows,

$$\left.\frac{\delta\lambda^{(p)}}{\lambda_0}\right|_{\delta a} \equiv D_0^{(p)} \cdot e^{-\gamma_p \cdot t} \cdot e^{-j\Omega_p \cdot t} \tag{4}$$

where $D_0^{(p)}$ is the magnitude of the relative wavelength shift that results from the geometrical contribution. Figure 2b shows $D_0^{(p)}$ experienced by the $TE_{358,1}$ and the $TM_{358,1}$ WGMs as a result of the oscillation of $R_{0,p}$ acoustic modes excited by a pump pulse of similar characteristics as in the previous section. Again, $R_{0,p}$ modes with even and odd p numbers produce a WGM resonance wavelength shift with opposite sign. Nearly identical results are obtained for both WGMs, as well as for WGMs with different radial orders.

It should be noted that, although not the largest values, the magnitude of the WGM wavelength shift produced by the lower order $R_{0,p}$ modes is significantly large. This feature is novel and remarkable since the contribution of the first radial modes is hardly noticeable in conventional interrogation methods based on the propagation of a probe beam through the fiber core.

2.3. Net WGM Wavelength Shift Due to $R_{0,p}$ Acoustic Modes

Finally, it should be noted that the two contributions to the WGM wavelength shift produced by a given $R_{0,p}$ mode, i.e., the contribution due to the material perturbation, and that of the geometric perturbation discussed in the previous sections, are of opposite sign, as expected. Therefore, they partially counteract each other. Figure 2c shows the overall relative wavelength shift of WGMs $TE_{358,1}$ and $TM_{358,1}$ caused by the different $R_{0,p}$ acoustic modes. The relative wavelength shift caused by radial acoustic modes with low order p is driven essentially by the geometric contribution, while for large p values is the photo-elastic effect that dominates. For $R_{0,p}$ radial modes for which the two contributions are of similar magnitude, the net effect on the WGM is minimum. As expected, the wavelength shift caused by any $R_{0,p}$ mode is different for the two WGMs evaluated mainly because of the different photo-elastic contributions. Thus, the modulation features that TAMRs will imprint on the probe signal will depend on the specific WGM used in the experimental implementation.

We would like to point out that, although the magnitude of the relative wavelength shift of the low-order $R_{0,p}$ modes is small (see Figure 2c), the contribution of these modes to the perturbation of the WGM resonance wavelength is quite significant. This is due to the attenuation of the different modes, which increases with the mode order. As it will be seen later, the linewidth of the

lower order modes is significantly smaller, almost two orders of magnitude smaller than that of higher order modes. Therefore, in the frequency domain, peaks that result from the oscillation of low order $R_{0,p}$ modes exhibit great amplitudes.

2.4. Coupling to WGMs in an Oscillating Cavity

The excitation and interrogation of WGM resonances of an opticalMR is typically done by evanescent field coupling from an auxiliary waveguide, in our case a thin fiber taper, which was positioned near or in contact with the MR. The amplitudes of the signal inside the MR and the transmitted signal through the auxiliary waveguide depend on the characteristics of the MR and the auxiliary waveguide, and also on the coupling between them. As described in detail above, the oscillation of an $R_{0,m}$ mode in the fiber causes the oscillation of the resonance wavelength of the WGMs of the fiber. This has implications on the excitation and interrogation of the WGMs since its resonance frequency is time dependent.

When an $R_{0,p}$ mode is oscillating in the fiber, the frequency difference between the optical field (the probe signal) and the WGM resonance frequency can be expressed as, $\Delta\omega\,(t) = \Delta\omega_{DC} + \Delta\omega_{AC} \cdot \cos\,(\Omega \cdot t)$, where $\Delta\omega_{DC}$ is the detuning in the absence of oscillation, $\Delta\omega_{AC}$ is the amplitude of the oscillation caused by the $R_{0,p}$ mode (investigated in the previous sections), and Ω is the oscillation frequency. In comparison with a static coupled system, the oscillation with time of the WGM resonance frequency introduces an oscillation on the amplitude of the wave transmitted through the fiber taper. In the steady state, for a small cavity perturbation and when the probe signal is tuned to the slope of the WGM resonance, the power of the transmitted signal can be described by,

$$T_{st}\,(t) \approx T_{DC} + \Delta T_{AC} \cdot \cos\,(\Omega \cdot \mathrm{t} + \phi) \tag{5}$$

where T_{st} is the steady-state transmittance, T_{DC} is the steady-state transmittance when there is no modulation of the cavity frequency, and ΔT_{AC} is the amplitude of the output power modulation due to the cavity perturbation. ΔT_{AC} depends on the strength of the cavity frequency modulation $\Delta\omega_{AC}$, and therefore it provides information about the amplitude of the acoustic oscillation inside the cavity. More details regarding this analysis can be found in the Supporting information.

We must note that ΔT_{AC} depends on the optical frequency ω, the Q factor of the WGM resonance, and on the frequency Ω at which the cavity oscillates. Such dependence on Ω is particularly interesting because it shows up the role of the Q factor of the WGM resonance. **Figure 3** shows ΔT_{AC}, computed for a constant $\Delta\omega_{AC}$, as a function of frequency $f\,(\Omega = 2\pi f)$ in the range of interest, for three different values of Q. We see that $\Delta T_{AC}(\Omega)$ has a low-pass filter response, in which the low frequency transmittance is proportional to the Q factor, while the cut-off frequency is inversely proportional to Q. This effect is particularly significant when ultranarrowband WGMs are used, i.e., ultra-high Q resonances. In order words, the sensitivity of the probing technique based on the transmittance of a fibered WGM resonance increases with the Q factor significantly enabling an optimized detection of lower order TAMRs, but when high bandwidth is required, then WGM resonances with lower Q factor should be chosen.

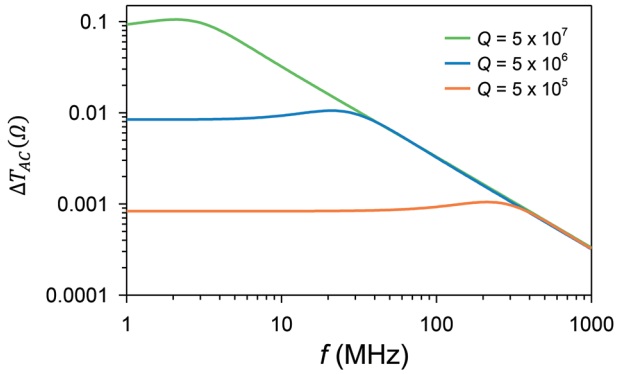

Figure 3. Modulation amplitude of the power transmittance ΔT_{AC} as a function of the cavity vibration frequency Ω. The three representative values of Q used in the calculations correspond to resonances' linewitdh of 30 fm, 300 fm and 3 pm, respectively, at the optical wavelength of 1.5 μm. An oscillation amplitude of $\Delta\,\omega_{AC} = 1 \times 10^6$ rad s^{-1}, which corresponds to a wavelength shift amplitude of 1.2 fm, was considered for the three cases.

3. Experimental Section

A schematic diagram of the experimental setup is shown in **Figure 4**a. A section of Fibercore SM1500-4.2/125 optical fiber (FUT) was used for the experiments reported here. The choice of this fiber as an acoustic resonator was based merely on comparative reasons with our previous experiments, in which we used this fiber.[37] Experiments were also performed on SMF-28 fiber and the results were pretty similar to those reported here. TAMRs of the FUT were generated by optical electrostriction using a pulsed diode laser (PDL). The emission characteristics of the PDL were: 1064 nm wavelength, 700 ps pulse duration, 19 kHz repetition rate, linear polarization (PER >20:1). The temporal shape of the pump pulses is shown in Figure 4a. The laser beam was delivered into the FUT using an aspheric lens (×16) and a 3-axis stage. Polarization control of the pump beam was not carried out.

WGMs of the FUT were excited and probed via the evanescent field of a thin tapered optical fiber of ≈3 μm diameter, fabricated from Corning SMF-28 fiber. The tapered fiber was positioned perpendicular to the FUT, in contact with it. This part of the experimental arrangement was placed inside of a methacrylate box to avoid dust contamination of the fiber taper and instabilities caused by air currents.

WGMs in a long cylindrical microresonator are delocalized, consequently, the circulating light beam that is evanescently coupled into the microresonator eventually radiates out along the cylinder axis. However, it has been shown that the self-interference of such a beam produces a resonant mode that is strongly localized along the axial direction, with Q-factor that can be almost as large as that of WGMs in a spheroidal microresonator.[45]

The light source used to this effect was a tunable diode laser (TDL) that emitted a narrow band (linewidth <30 kHz), linearly polarized beam in the C-band. A fiber polarization controller was included to adjust the polarization state of the light in the fiber ta-

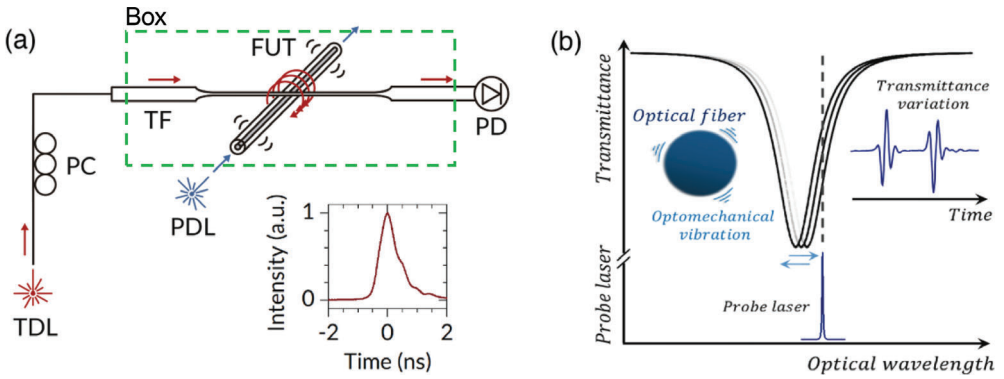

Figure 4. a) Experimental setup. TDL: tunable diode laser; PC: polarization controller; PDL: pulsed diode laser; PD: photodiode; OSC: oscilloscope; TF: tapered fiber. Inset shows the temporal profile of the pump pulses. b) Schematic illustration of the probing method.

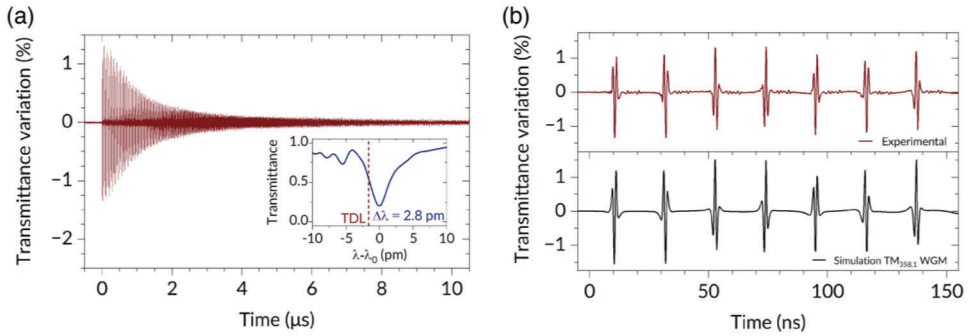

Figure 5. Temporal response of the probe laser transmittance after a pump pulse propagated along the FUT. a) Full time span showing the decay of the oscillations. Inset shows the spectrum of the $TM_{358,1}$ WGM. b) A detail just after $t = 0$. Experimental (top) and theoretical simulations (bottom). Pump pulse peak power: 6 kW.

per in order to excite *TE*- and/or *TM*-polarized WGM resonances. The TDL integrated a piezoelectric-based fine-frequency tuning facility that allowed continuous scanning around a given wavelength. The excitation of a WGM in the FUT lead to a notch in the spectrum of the light transmitted through the fiber taper, as it is depicted in **Figure 4**b.

The TDL was precisely tuned to a spectral slope of the WGM notch. Then, the wavelength modulation of the WGM notch was converted into an intensity-modulated signal that was detected and recorded using a fast photodetector and an oscilloscope. Demodulation of the probe signal to quantify the characteristics of the TAMRs is straightforward as long as the WGM notch oscillation is such that the laser always remains tuned to the linear part of the notch. Then, only the slope of the notch needs to be known, and the relationship between the probe signal modulation and the amplitude of the TAMRs oscillation is proportional. When such linear detection regime cannot be accomplished, detection of TAMRs is still feasible, but quantification of the TAMRs induced perturbation would be more complicated.

Environmental fluctuations and vibrations cause slow wavelength drift/oscillation of the WGM resonance. Therefore, to keep the probe laser tuned to the linear slope of the WGM resonance during the measurements, an active locking technique based on an electronic feedback control system was implemented and used to assist locking of the probe laser wavelength to the WGM notch.[43]

4. Results

We first focus on measurements performed with relatively low Q factor WGMs in order to ensure a broadband frequency response consistent with the results reported in Figure 3. In particular, the spectrum of one of the WGMs used in these experiments is shown in **Figure 5**a, the notch is located at 1535.9 nm, it exhibits a 3dB-bandwidth of 2.8 pm and a quality factor of 6.4×10^5. This notch corresponds to the excitation of the $TM_{358,1}$ WGM. The results included in the paper were obtained using the $TM_{358,1}$ and $TE_{358,1}$ WGMs. Among the large number of WGMs supported by the optical fiber, the choice of those WGMs was motivated by the following points: 1) modes with radial number $n = 1$ were preferred because they exhibit a narrower resonance and they have simpler electromagnetic field profile, and 2) the tuning bandwidth of our tunable laser (1530 nm – 1545 nm). Since the free spectral range in the optical fiber is about 4 nm, other WGMs with radial number $n = 1$ could have been used with similar performance.

Figure 5a,b show an example of the transmittance oscillation of the probe signal recorded after one pump pulse propagated along the fiber at $t = 0$. Signal averaging was applied to improve the signal-to-noise ratio. The amplitude modulation of the probe signal indicates the wavelength oscillation of the WGM notch.

The RF spectra of the probe signals obtained with the $TM_{358,1}$ and with the $TE_{358,1}$ WGMs are shown in **Figure 6**a,b,

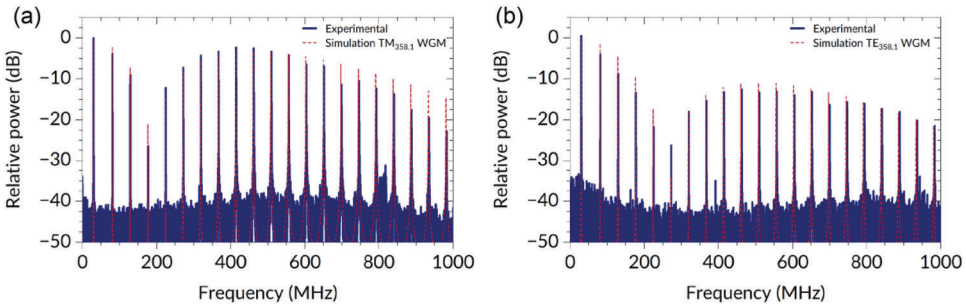

Figure 6. Normalized RF spectrum of the probe signal after a pump pulse propagated along the FUT when probing with a) the $TM_{358,1}$ and b) the $TE_{358,1}$ WGM. Pump pulse peak power: 6 kW. The corresponding theoretical simulation are included as red dashed line.

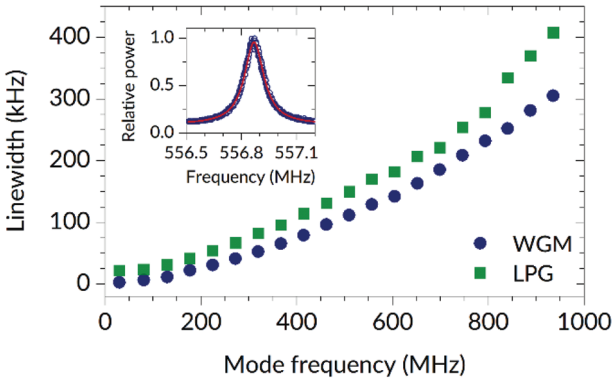

Figure 7. Linewidth of $R_{0,p}$ modes as a function of their resonance frequency. Dots are for the present technique and squares are the results reported in [34]. The inset shows the spectrum of the $R_{0,12}$ resonance and the corresponding fitting curve.

respectively. A series of quasi equally-spaced peaks that extends beyond 1 GHz is shown. Each peak results from the interplay of an $R_{0,p}$ radial mode with the corresponding WGM. In both RF spectra, the envelope shows a minimum, which occurs in different radial modes for both WGMs. Specifically, the peak of minimum amplitude in the spectrum obtained with the $TM_{358,1}$ WGM corresponds to the $R_{0,4}$ acoustic mode, while in the spectrum obtained with the $TE_{358,1}$ WGM, the minimum is produced by the $R_{0,6}$ acoustic mode.

The amplitude of the different peaks of the RF spectrum was proportional to the pump power delivered into the FUT. Measurements were performed for an average pump power ranging between 2 and 85 mW, which correspond to pulse peak power of 146 W and 6.2 kW. For the lowest pump power level, and the $TM_{358,1}$ the amplitudes of the peaks corresponding to the $R_{0,1}$ and $R_{0,10}$ modes were 15 and 12 dB above the noise level.

High-resolution spectra of individual $R_{0,p}$ modes were measured using a RF signal analyzer. The linewidth of the resonances was obtained by fitting a Lorentzian function to the spectrum of each resonance. An example is shown in the inset of **Figure 7**. The result obtained for the different $R_{0,p}$ acoustic modes is shown in Figure 7.

We investigated experimentally the effect of the Q factor of the WGM resonance used for probing the TAMRs. By applying a thermal treatment to the fiber, the surface roughness and surface contaminants can be reduced, which can be used to enhance the Q factor of the WGMs.[43] Following this strategy, we could perform experimental measurements with the same WGM but different Q factor values. For comparison purposes with the results shown previously in Figures 5 and 6, we carried out measurements with the $TM_{358,1}$ WGM. In the first step, the spectral bandwidth of the WGM resonance was reduced from 2.8 pm (Q factor 6.4×10^5) to 465 fm (Q factor 3.3×10^6), and in a second step it was further reduced to 92 fm (Q factor 1.7×10^7). **Figure 8** summarizes the obtained results. For each case, the WGM spectrum, an interval of the temporal trace of the probe signal, and the RF spectrum are shown. The experimental conditions, including the pump power, were similar as in the experimental measurements shown in Figures 5 and 6.

5. Discussion

The temporal trace shown in Figure 5a,b contains a sequence of beats separated by ≈21 ns with amplitude decaying with time. The sequence of beats results from the joint contribution of higher order $R_{0,p}$ modes; the roundtrip time of an acoustic pulse traveling in the radial direction across the fiber (125 µm diameter) at the longitudinal acoustic velocity (≈5960 $m^{-1}s$) agrees with the period of the beats. The transmittance variation can be correlated with the wavelength shift of the WGM notch. As an example, the amplitude of the first transmittance oscillation is ≈1.3%, which corresponds to a wavelength shift of the WGM resonance of ≈42 fm.

As shown in Figure 5b, the probe signal trace does not show any sign of the contribution of XPM due to instantaneous Kerr effect. When XPM happens, large modulation of the probe signal is observed from $t = 0$, while in Figure 5b it is shown that before the first oscillation that takes place ≈10.5 ns after the pump pulse, the probe does not show any modulation at all. In fact, no evidence of XPM was observed in the range of pump power available in our experiment, with a maximum peak power delivered into the fiber of 6 kW.

In the RF spectra of the probe signal for both WGMs (Figure 6a,b), the peak with the highest intensity corresponds to the contribution of the $R_{0,1}$ mode. This is a remarkable difference when comparing with previous methods for probing the TAMRs in which the first $R_{0,p}$ modes were weakly detected.[23,37–38] Attending to the analysis carried out in the previous section, this result demonstrates the geometric perturbation effect produced by TAMRs in the fiber, since the contribution of the refractive

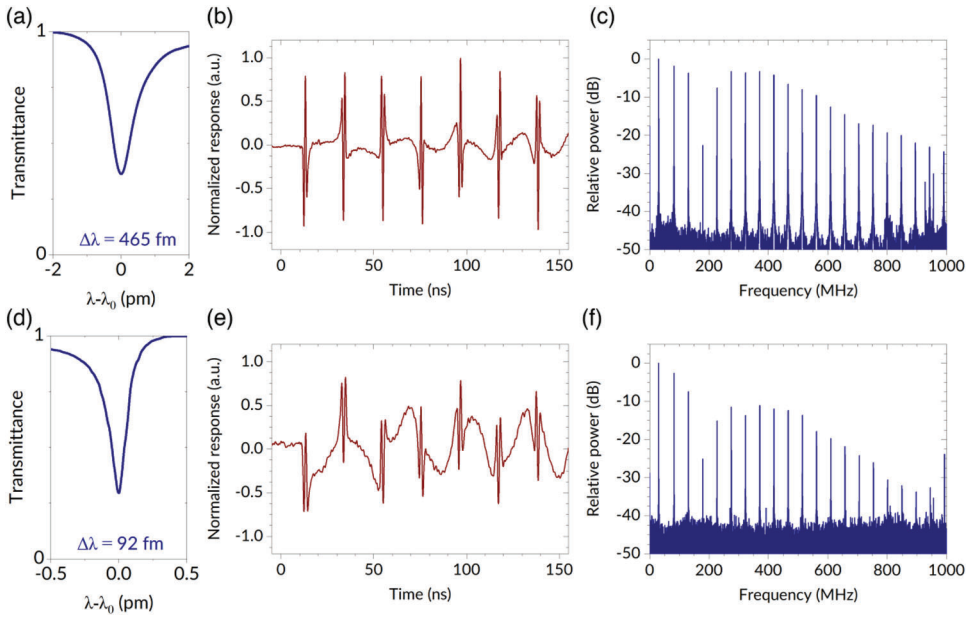

Figure 8. WGM spectrum (left, (a,d)). An interval of the temporal trace of the probe signal just after a pump pulse propagates through the FUT at $t = 0$ (center, (b,e)). RF spectrum of the probe signal (right, (c,f)).

index perturbation induced by the $R_{0,1}$ mode is rather small (see Figure 2).

The envelope of the RF spectra shows a minimum in amplitude. As discussed in the previous section, it results from the opposite sign of the two contributions to the WGM wavelength shift. If the geometrical and the refractive index contributions are of similar magnitude, one almost counteracts the other. For the specific WGMs used for this measurement, the peak with lowest amplitude corresponds to the $R_{0,4}$ mode for $TM_{358,1}$ and to the $R_{0,6}$ mode for $TE_{358,1}$. Probing the TAMRs with WGMs of different radial order was carried out experimentally. We observed that the relative amplitude profile of the series of peaks in the RF spectrum changed, as well as the peak of minimum amplitude, in line with the theoretical calculations.

Finally, we would like to remark that frequency components related to torsional-radial $TR_{2,m}$ modes were not observed in any case.

The linewidth of the resonances obtained by the present method can be compared with those reported previously by other probing methods. With this purpose, we have included in Figure 7 the linewidth values of optical fiber TAMRs reported in,[36] which had been the lowest reported prior to this work. The linewidth values measured with the present technique are ≈25% smaller. Therefore, we can conclude that the linewidth of the TAMRs provided by the present method is, to our knowledge, the smallest ever reported. We believe that this is related to the small extension of the probe light beam on the fiber under test – the extension of the WGM fields in the axial direction is estimated to be ≈200 μm[45] – which reduces the contribution to linewidth broadening due to fiber inhomogeneities.

When comparing the probe signal modulation obtained with the WGM of different Q factor, the general trend described in Figure 3 is confirmed. The contribution of low frequency harmonics to the temporal trace is more noticeable as the Q factor of the WGM used for the measurement increases. This effect can be related to the increase of the slope of the WGM resonance. For example, a clear modulation of ≈30 MHz, caused by the $R_{0,1}$ mode, can be seen in the oscilloscope traces depicted in Figure 8b,e. In addition, as Q factor increases, the amplitude of the higher-order resonances fades away. The origin of such an effect is the low-pass filter response described above, which attenuates the higher frequency contributions, as can be seen in the RF spectra.

Following the theoretical concepts described in previous sections, we calculated theoretically the modulation of the probe signal. First, we evaluated the modulation of the WGM resonance wavelength caused by the series of $R_{0,p}$ acoustic modes excited by a pump pulse. Then, assuming a linear slope of the WGMs notch edge, and taking into account the equalization effect of the transmittance due to the cavity oscillation in the taper-MR coupled system, the intensity modulation of the probe signal was finally calculated in the time- and in the frequency-domain, for the two WGMs used in the experiments. The theoretical calculations are in excellent agreement with the experimental observations. The results of the theoretical calculations for the specific parameters and conditions of the experiments are included in Figure 5b (temporal trace), and in Figure 6 (RF spectra).

6. Conclusion

In this work, we have shown that the interplay between optical and acoustic resonances can be exploited to investigate high-frequency opto-excited transverse acoustic mode resonances in optical fibers. The oscillation of a TAMR introduces a small perturbation both in the dielectric permittivity and in the geometry of the fiber, in the latter case affecting the cross-section radius. Such perturbations, although small, affect significantly the fields of the WGMs. The perturbation produced by radial acoustic resonances $R_{0,p}$ results in the modulation of the WGM fre-

quencies of resonance. We have shown that $R_{0,p}$ modes can be interrogated and detected efficiently by monitoring the WGM resonances. The development of a model to describe the transmittance of the fibered WGM resonator permits an accurate analysis of the interplay between sensitivity, bandwidth and the Q factor of the WGM resonance. We have also shown that the WGM resonance wavelength is not sensitive to torsional-radial $TR_{2,p}$ acoustic modes.

Full characterization of opto-excited $R_{0,p}$ modes was performed by this method. Experimental results confirmed that the contribution of the two type of perturbations, i.e., the geometric and the photo-elastic perturbations, are equally relevant. The lower order opto-excited $R_{0,p}$ modes produce large modulation of the WGMs, thus they can be interrogated accurately by this technique, while they are hardly detected with previously reported probing techniques based on core perturbations. The linewidth of the acoustic resonances obtained by this method is remarkably shorter than previously reported. We believe that this is related to the small extension of the probe light beam on the fiber under test, which reduces the contribution to linewidth broadening due to fiber inhomogeneities.

Our results reinforce the potential of future developments based on combining acoustic and optical resonances in a single device.

Supporting Information

Supporting Information is available from the Wiley Online Library or from the author.

Acknowledgements

This work has been supported in part by the European Regional Development Fund (PID2019-104276RB-I00); the European Commission (H2020-MSCARISE-2019-872049); Generalitat Valenciana (IDIFEDER/2020/064, CIPROM/2022/30); and the Ministerio de Ciencia, Innovación y Universidades (PID2019-104276RB-I00).

Conflict of Interest

The authors declare no conflict of interest.

Data Availability Statement

The data that support the findings of this study are available from the corresponding author upon reasonable request.

Keywords

forward Brillouin scattering, optical fibers, optical microresonators, optomechanics, whispering-gallery modes

Received: July 13, 2023
Revised: September 10, 2023
Published online:

[1] D. Culverhouse, F. Farahi, C. N. Pannell, D. A. Jackson, *Electron. Lett.* **1989**, *25*, 913.
[2] M. Delgado-Pinar, D. Zalvídea, A. Díez, P. Pérez-Millán, M. V. Andrés, *Opt. Express* **2006**, *14*, 1106.
[3] E. Alcusa-Sáez, A. Díez, M. V. Andrés, *Opt. Express* **2016**, *24*, 4899.
[4] A. Denisov, M. Soto, L. Thévenaz, *Light Sci Appl* **2016**, *5*, e16074.
[5] J. Lu, F. Shi, J. Xu, L. Meng, L. Zhang, P. Cheng, X. Zhou, F. Pang, X. Zeng, *Nanophotonics* **2021**, *10*, 983.
[6] M. Merklein, B. Stiller, K. Vu, S. J. Madden, B. J. Eggleton, *Nat Commun* **2017**, *8*, 574.
[7] B. J. Eggleton, C. G. Poulton, P. T Rakich, M. J. Steel, G. Bah, *Nat. Photonics* **2019**, *13*, 664.
[8] T. Carmon, H. Rokhsari, L. Yang, T. J. Kippenberg, K. J. Vahala, *Phys. Rev. Lett.* **2005**, *94*, 223902.
[9] T. Carmon, K. J. Vahala, *Phys. Rev. Lett.* **2007**, *98*, 123901.
[10] X. Roselló-Mechó, D. Farnesi, G. Frigenti, A. Barucci, A. Fernández-Bienes, T. García-Fernández, F. Ratio, M. Delgado-Pinar, M. V. Andrés, G. Nunzi-Conti, S. Soria, *Sci. Rep.* **2019**, *9*, 7163.
[11] T. J. Kippenberg, R. Holzwarth, S. A. Diddams, *Science* **2011**, *332*, 555.
[12] S. Spillane, T. Kippenberg, K. Vahala, *Nature* **2002**, *415*, 621.
[13] M. Humar, S. H. Yun, *Nat. Photonics* **2015**, *9*, 572.
[14] J. Zhu, S. K. Ozdemir, Y. F. Xiao, L. Li, L. He, D. R. Chen, L. Yang, *Nat. Photonics* **2009**, *4*, 46.
[15] X. Rosello-Mecho, M. Delgado-Pinar, A. Díez, M. V. Andrés, *Opt. Lett.* **2016**, *41*, 2934.
[16] E. Rivera-Pérez, I. L. Villegas, A. Díez, M. V. Andrés, J. L. Cruz, A. Rodríguez-Cobos, *IEEE Photon. Technol. Lett.* **2013**, *25*, 2498.
[17] X. Rosello-Mecho, M. Delgado-Pinar, A. Díez, M. V. Andrés, *Opt. Lett.* **2018**, *43*, 2897.
[18] R. M. Shelby, M. D. Levenson, P. W. Bayer, *Phys. Rev. B* **1985**, *31*, 5244.
[19] A. J. Poustie, *J. Opt. Soc. Am. B* **1993**, *10*, 691.
[20] A. S. Biryukov, M. E. Sukharev, E. M. Dianov, *Quantum Electron.* **2002**, *32*, 765.
[21] H. Shin, W. Qiu, R. Jarecki, J. A. Cox, R. H. Olsson III, A. Starbuck, Z. Wang, P. T. Rakich, *Nat. Commun.* **2013**, *4*, 1944.
[22] G. S. Wiederhecker, Pa. Dainese, T. P. Mayer Alegre, *APL Photonics* **2019**, *4*, 071101.
[23] Y. Antman, A. Clain, Y. London, A. Zadok, *Optica* **2016**, *3*, 510.
[24] Y. London, K. Sharma, H. H. Diamandi, M. Hen, G. Bashan, E. Zehavi, S. Zilberman, G. Berkovic, A. Zentner, M. Mayoni, A. A. Stolov, M. Kalina, O. Kleinerman, E. Shafir, A. Zadok, *J Lightwave Technol* **2021**, *39*, 6637.
[25] L. A. Sánchez, A. Díez, J. L. Cruz, M. V. Andrés, *Opt. Express* **2022**, *30*, 14384.
[26] K. Shemer, G. Bashan, E. Zehavi, H. H. Diamandi, A. Bernstein, K. Sharma, Y. London, D. Barrera, S. Sales, A. Bergman, A. Zadok, *Opt. Express* **2022**, *30*, 39321.
[27] L. A. Sánchez, A. Díez, J. L: Cruz, M. V. Andrés, *Sensors* **2023**, *23*, 318.
[28] D. M. Chow, L. Thévenaz, *Opt. Lett.* **2018**, *43*, 5467.
[29] G. Bashan, H. H. Diamandi, Y. London, E. Preter, A. Zadok, *Nat. Commun.* **2018**, *9*, 2991.
[30] D. M. Chow, Z. Yang, M. A. Soto, L. Thévenaz, *Nat. Commun.* **2018**, *9*, 2990.
[31] H. H. Diamandi, Y. London, G. Bashan, A. Zadok, *APL Photonics* **2019**, *4*, 016105.
[32] C. Pang, Z. Hua, D. Zhou, H. Zhang, L. Chen, X. Bao, Y. Dong, *Optica* **2020**, *7*, 176.
[33] L. A. Sánchez, A. Díez, J. L. Cruz, M. V. Andrés, *Opt. Express* **2022**, *30*, 42.
[34] Zijie Hua, Dexin Ba, Dengwang Zhou, Yijia Li, Yue Wang, Xiaoyi Bao, Yongkang Dong, *Light: Adv. Manufact.* **2021**, *2*, 25.
[35] G. Bashan, H. H. Diamandi, E. Zehavi, K. Sharma, Y. London, A. Zadok, *Nat. Commun.* **2022**, *13*, 3554.
[36] G. Bashan, H. H. Diamandi, Y. London, K. Sharma, K. Shemer, E. Zehavi, A. Zadok, *Light Sci Appl* **2021**, *10*, 119.
[37] L. A. Sánchez, A. Díez, J. L. Cruz, M. V. Andrés, *Opt. Lett.* **2020**, *45*, 5331.

[38] H. H. Diamandi, Y. London, A. Bergman, Gil Bashan, J. Madrigal, D. Barrera, S. Sales, A. Zadok, *IEEE J. Sel. Top. Quantum Electron.* **2020**, *26*, 2600113.
[39] Jing Wang, Yunhui Zhu, Rui Zhang, Daniel J. Gauthier, *Opt. Express* **2011**, *19*, 5339.
[40] L. Arques, A. Carrascosa, V. Zamora, A. Díez, J. L. Cruz, M. V. Andrés, *Opt. Lett.* **2011**, *36*, 3452.
[41] D. M. Pozar, *Microwave Engeneering*, 4th ed., Wiley, New York **2001**.
[42] G. Annino, M. Cassettari, I. Longo, M. Martinelli, *IEEE Trans. Microwave Theory Tech.* **1997**, *45*, 2025.
[43] T. Carmon, T. J. Kippenberg, L. Yang, H. Rokhsari, S. Spillane, K. J. Vahala, *Opt. Express* **2005**, *13*, 3558.
[44] M. L. Gorodetsky, A. A. Savchenkov, V. S. Ilchenko, *Opt. Lett.* **1996**, *21*, 453.
[45] M. Sumetsky, *Opt. Lett.* **2010**, *35*, 2385.